Reversible Planar Gliding and Microcracking in Single Crystalline Ni-rich Cathode for Advanced Li-ion Batteries

Yujing Bi,[1] Jinhui Tao,[1] Yuqin Wu,[2,4] Linze Li,[1] Yaobin Xu,[1] Enyuan Hu,[3] Bingbin Wu,[1] Jiangtao Hu,[1] Chongmin Wang,[1] Ji-Guang Zhang,[1] Yue Qi,[2,4] Jie Xiao [1,5]*

[1]Pacific Northwest National Laboratory, Richland, WA 99352, USA

[2]School of Engineering, Brown University, Providence, RI 02912, USA

[3]Chemistry Division, Brookhaven National Laboratory, Upton, NY 11973, USA

[4]Department of Chemical Engineering and Materials Science, Michigan State University, East Lansing, MI 48824, USA

[5]Materials Science and Engineering Department, University of Washington, Seattle, WA 98195, USA

*Correspondence to: jie.xiao@pnnl.gov

Abstract: Single crystalline Ni-rich cathode materials have a great potential to address the challenges present in their polycrystalline counterparts in terms of moisture sensitivity, side reactions and gas generation, all of which initiate from materials surfaces. However, a fundamental understanding is lacking on the relationship between over potential, microstructure and electrochemical behaviors in single crystalline Ni-rich cathodes. We observe reversible planar gliding and microcracking along the (003) plane in a single crystalline Ni-rich cathode. The reversible formation of microstructure defects are correlated with the localized stresses induced by a concentration gradient of Li atoms in the lattice, providing clues to mitigate particle fracture from synthesis modifications.

One Sentence Summary: Reversible gliding and microcracking of lattice planes are observed in single crystalline Ni-rich cathode materials.

For long-range electrical vehicles, next-generation Li-ion batteries employing stable high-energy cathode materials are urgently needed (*1*). Among different cathodes, Ni-rich NMC ($LiNi_xMn_yCo_{1-x-y}O_2$, x > 0.6), with > 200 mAh/g capacity, high voltage (>3.8V) and low cost, are considered as one of the most promising candidates (*2*). Traditional $LiNi_{1/3}Mn_{1/3}Co_{1/3}O_2$ cathodes are prepared using a co-precipitation method which aggregates nano-sized primary particles into micron sized secondary particles. The agglomerated polycrystalline NMC have shortened diffusion lengths within their primary particles and increased number of pores, which accelerates Li^+ transport and thus becomes the most popular morphology for conventional NMC particles (*3*).

Creating spherical-secondary polycrystalline NMC particles reduces the surface/volume ratio, but pulverization along the weak internal grain boundaries are generally observed after cycling (*4*). These cracks are induced by the non-uniform volume change of primary particles during cycling and exacerbated by the anisotropy among dividual particles and grains in the polycrystalline NMC (*5*). The intergranular cracking exposes new surfaces to electrolyte for side reactions which accelerates cell degradation (*6*). As the Ni content increases to more than 0.6, e.g., $LiNi_{0.8}Mn_{0.1}Co_{0.1}O_2$, usable capacity is further increased but new challenges such as moisture

sensitivity (*7*), aggressive side reactions and gas generation (*8*) during cycling are found, all of which initiate from particle surfaces.

A feasible approach for stabilizing Ni-rich NMC is to synthesize single crystalline cathodes with reduced surface areas, phase boundaries and more integrated crystal structures, similar to $LiCoO_2$ (*9*). Single crystalline NMC with Ni≤0.6 presenting good performances has been demonstrated (*10-17*). However, the capacity of those single crystal NMC (Ni≤0.6) is relatively low due to the limited Ni content. Single crystalline Ni-rich cathodes with Ni>0.6 substantially increases the capacity but are not much reported (*18, 19*) due to the challenges of preparing high-performance Ni-rich NMC single crystals. Owing to low structure stability of Ni-rich cathode at high temperatures, higher Ni content cathodes require lower synthesis temperatures, opposite to the high-temperature and long-time calcination process required to grow single crystals. Synthesis of stoichiometric single crystal with competitive electrochemical properties is a challenge (*20*).

This work utilizes high-performance single crystalline $LiNi_{0.76}Mn_{0.14}Co_{0.1}O_2$ (NMC76) as a model material to study how the potential triggers the structural changes of single crystals from the atomic to micron scale and its implications to the electrochemical properties of cathodes. In situ atomic force microscopy (AFM) and theoretical modeling are utilized to understand the coupled electro-chemo-mechanical behaviors of single crystals.

The synthesized NMC76 has an average particle size of 3 μm (Fig. 1A). A cross-section view (Fig. 1B) shows that NMC76 has a dense structure without cavities or grain boundaries. Pure phases of α-$NaFeO_2$-type layered structures are confirmed by both selected area electron diffraction (SAED, Fig. 1C) and X-ray Diffraction (XRD, Fig. 1D). Lattice parameters *a* and *c* are 2.8756(1) Å and 14.2221(1) Å, respectively, from Rietveld refinement (see details in Table S1). For comparison, polycrystalline NMC76 are found to contain many internal pores and intergranular boundaries along with surface films (Fig. S1) formed from the reactions between NMC and air *(7)*. In contrast, the surface of single crystalline NMC76 is very uniform (Fig. 1E and 1F). Elemental mapping (Fig. 1G and 1H) indicates a homogeneous distribution of Ni, Mn and Co with a stoichiometric ratio as designed (Fig. S2, Table S2). Continuous phase transitions happen when potential changes (Fig. S3), similar to polycrystalline NMC76 (*21*).

Single crystalline NMC76 is further tested in graphite/NMC full cells at realistic conditions. The typical loading of NMC76 cathodes is ca. 20 mg/cm^2 (=4 mAh/cm^2) with ca. 32% porosity, which is needed to build a 250 Wh/kg Li-ion cell (see Table S3 in Supplementary Materials). Jeff's earlier work also presented a wide range of testing results of Li-ion batteries based on graphite/$LiNi_{0.5}Mn_{0.3}Co_{0.2}O_2$ chemistry *(16)*, which can serve as benchmarks for academic research. The electrode properties in terms of loading etc in Jeff's work are similar to ours since both are derived from realistic pouch cell parameters. At such a high cathode loading, Li metal will worsen the cycling stability (Fig. S4 and S5) due to the deepened stripping/deposition process of Li. Between 2.7 and 4.2 V (*vs.* Graphite), single crystalline NMC76 delivers 182.3 mAh/g discharge capacity at 0.1C, and retains 86.5% of its original capacity after 200 cycles (Fig. 2A1). With a cutoff of 4.3 V, single crystalline NMC76 delivers 193.4 mAh/g capacity with 81.6% capacity retention after 200 cycles (Fig. 2A2). Further increasing to 4.4 V, 196.8 mAh/g discharge capacity is seen (Fig. 2A3) along with a 72.0% capacity retention after 200 cycles. Note that 200 cycles at C/10 charge rate and C/3 discharge rate mean 2600 hours of cycling. The total testing time is equal to a cell undergoing 1300 cycles at 1C. To evaluate the electrochemical properties of materials, it is important to use a relatively slow rate rather than a very fast rate which produces seemly "longer" cycles but may "hide" critical electrochemical information. It is the total time of

charge/discharge matters instead of cycling number (*22*). Increased polarization (Fig. 2B1, 2B2, 2B3) is observed when the cutoff voltage increases which is presumably assigned to intensified electrolyte decomposition at elevated voltages (Fig. S6-S8) and thus higher impedance resulting from cathode passivation films and single crystal lattice change. Table S4 summarizes the electrochemical performances and testing conditions of all previously published single crystalline Ni-rich NMC (Ni > 0.6) cathode materials.

Lattice gliding is clearly observed in single crystalline NMC76 at high voltages. Between 2.7 and 4.2 V, the entire single crystal is well maintained after 200 cycles (Fig. 2C1). Increasing cutoff voltage to 4.3 V, there are some gliding lines seen on the crystal surfaces after 200 cycles (Fig. 2C2). Cycled to 4.4 V, single crystals appeared to be "sliced" (Fig. 2C3 and Fig. S9) in parallel, along the (003) plane and vertical to *c*-axis of the layered structure (Fig. 3C), which indicates a model II type crack (in-plane shear) in fracture mechanics (*23*). Additionally, small cracks that indicate a model I type fracture (opening) are also discovered at 4.4 V (Fig. 2C3). All characterizations have been done by selecting various regions of NMC76 electrodes and the same phenomenon is repeatedly found (Fig. S10-S12). Although single crystalline NMC76 as a whole particle is still intact (Fig. 3A), gliding is the major mechanical degradation mode especially when cutoff voltage is above 4.3 V. Of note, the "gliding steps" formed in cycled crystals are quite different from cracking along intergranular boundaries of polycrystalline NMC particles (*24*). The scanning transmission electron microscopy (STEM) image for single crystalline NMC76 (Fig. 3B, 3C, 3D, 3E) confirms that on both sides of a gliding plane (yellow line in Fig. 3D), the *d*-spacing of (003) plane (0.48 nm) is unchanged and the layered structure is well maintained after the "gliding" marks occur. The long-range lattice symmetry of the bulk material will thereby not be altered (Fig. S13). Ni, Mn, Co and O are still uniformly distributed in the vicinity of glided planes based on electron energy loss spectroscopy (EELS) analysis (Fig. 3F and Fig. S14). The uniform element distribution and intimately attached lattices across the gliding planes strongly demonstrate that although planar gliding occurs, no new boundary is generated, and the "sliced" area maintains the same lattice structure and chemical conditions as in the bulk phase. It should be noted that the gliding line (or the slicing marks) cannot be observed on the cross section of bulk particles by SEM, and are only visible by STEM bright field (BF) on thin sliced TEM samples. Although the internal lattice symmetry is well maintained after the gliding, the repeated gliding near surface eventually will evolve into microcracks exposing new surfaces to the electrolyte (Fig. 2).

To further induce lattice gliding, the cutoff voltage of NMC76 single crystal is raised to 4.8 V (*vs.* Li^+/Li). "Slicing marks" and microcracks are present in almost every charged single crystal (Fig. S15A). Slight deformation of individual single crystals is clearly observed (Fig. 3G), probably because the gliding of each layer equally likely moves towards symmetrically equivalent directions (*25*). Surprisingly, after discharging back to 2.7 V, the majority of single crystals revert to their original morphologies and the previously observed steps and microcracks disappear (Fig. S15B). The "glided" layers within single crystals almost completely "glided" back to their original locations (Fig. 3H), fully recovering from the deformation (Fig. 3G), although some "traces" are visible (labeled in Fig. 3H). Within the "regular" electrochemical window of 2.7 - 4.4 V (*vs.* Graphite), after extensive cycling, lattice gliding and microcracking are also seen within crystal lattice at charged status (Fig. 3I). STEM analysis of the NMC76 crystal (Fig. 3J) indicates that the microcracks initiate from inside of the crystal. At the discharge status of those cycled crystals (cut off at 4.4 V), few ridges or cracks are found on the crystals. Although not as visible as in charged crystals, STEM still uncovers some "slicing marks" (Fig. 3K) on discharged single crystal NMC76

which probably undergoes reversible "sliding" process back and forth during 120 cycles. No microcracking is identified in those "self-healed" single crystals (Fig. 3L), suggesting that the lattice gliding and cracking in some of the crystals are still reversible after 120 cycles. As cycling continues, particle deformation will become dominant. Dislocation is also observed near the tip regions of microcarck of single crystals charged at 4.4 V (Fig. S16). The accumulation of dislocation is accompanied by the microcrack propagation (*26*). A trace amount of nano-sized NiO-like rock salt phase (Fig. S17) is observed on the gliding exposure step area of single crystalline NMC76 after cycling.

In situ AFM has been used to image the crystal surface in real time in an electrochemical cell. A ~3 μm sized NMC76 single crystal is studied by in situ AFM during charge and discharge (Fig. 4). Regions B and C in Fig. 4A are enlarged in Fig. 4B and 4C, respectively, to probe the origin and evolution of "gliding steps" and microcracks under the electrical field. The formation of nanosized crack domains is observed on the side surface from open circuit voltage (OCV)to 4.50 V (*vs.* Li^+/Li) during charge, while these domains disappear in the discharge process (Fig. 4B). Moreover, planar gliding is characterized by the appearance of wide crystal steps on the side surface due to the uneven movement between neighboring layers during polarization. More wide gliding steps are observed on the side surface starting at 4.20 V charging process and lead to the more and wider (~ 85 nm) gliding steps at 4.50 V (Fig. 4C). When the cell potential decreases to 4.19 V, a few wide gliding steps decrease in their width (Fig. S18), indicating the atomic layer recovers back to their original position (Fig. 4C). The movie of in situ AFM showing the reversible and continuous morphological changes during charge and discharge is available in Supplementary Materials (Movie S1). The reversible gliding process is further illustrated in Fig. 4F. The observed lattice gliding is a direct observation of the "Lattice-Invariant Shear (LIS)" (*25*). LIS should exist in many layered electrode materials, which experience stacking-sequence-change phase transformations due to lithium concentration change. It was also predicted that LIS will lead to particle deformation and ridges on the particle surface, but these signals are likely to be buried in the internal boundaries in a spherical-secondary polycrystalline. The micron-sized single crystal provides a clear platform to observe gliding or LIS induced mechanical degradation.

Electrochemical potential difference is the driving force of lithium-ion diffusion and the formation of the lithium concentration gradient (*27*). Stress will be generated during Li^+ diffusion after establishing a lithium concentration gradient in the lattice. An analytical cylindrical isotropic diffusion-induced stress model is applied to understand the stress generation when lithium ions diffuse along the radial direction in the particle (Fig. S19). The peak tensile stress along tangential and axial directions occur near the surface at the onset of delithiation during charge (Fig. S20). Conversely, the peak tensile stress in all three directions occurs at the center of the particle (Fig. S21) during lithiation. During charge (delithiation), the tensile stress along axial and tangential directions is localized on the surfaces of single crystals, leading to microcrack opening normal to (003) planes.

Local stress also has shear component along other directions, which is solved numerically via COMSOL. The shear stress component along yz direction that can trigger the gliding along the (003) planes is shown in Fig. 4D and 4E. Although the sign of the shear stress during lithiation and delithiation is opposite which explains the reversible gliding, the absolute values are not the same (Fig. S22), since the elastic modulus is a function of Li concentration (*28*). Therefore, the gliding motion should be largely but not completely reversible. The irreversible gliding can generate small damages, being accumulated into the crack opening over long time cycling, an

analog of fatigue crack nucleation. These lead to the ridges and microcracks seen on the surfaces of single crystals.

The simple isotropic diffusion-induced-stress model can be used to predict if the cracks can be stabilized inside of the single crystal. Since the strain energy inside the particle reaches a maximum around the scaled time of T_p=0.1T during delithiation (Fig. 20), its comparison with the fracture energy (2γ) is used as a criterion to evaluate the critical size of single crystal NMC76 (*28*). If the accumulated strain energy is not large enough to cleave entire the crystal, the crack will be stabilized inside of the particle.

$$\Pi|_{T_p} = \int \frac{\sigma^2}{2E} dV = \pi * h * \left[\frac{\alpha * E_0 * (C_R - C_0)}{1-\nu}\right]^2 * \int_0^r \xi^2 \frac{1}{E} r dr < 2\gamma \qquad (1)$$

where h is the height of the cylindrical particle, α is the concentration expansion coefficient, E_0 is Young's modulus of the nonlithiated particle, E is Young's modulus at a given lithium-ion concentration, C_R is the lithium-ion concentration at the surface, C_0 is the lithium-ion concentration at the center, ν is Poisson's ratio and ξ represents the dimensionless stress (Fig. S19-S21), and γ is the surface energy, these values are listed in the SI. A lower bound estimation of the critical size of the single crystal is predicted to be ~3.5 μm, below which cracks can be considered stable inside of the particle. The simulation result suggests that although fractures along (003) direction appear in single crystals during cycling, the cracks are stable once formed and will not initiate catastrophic reactions to produce a fracture zone that eventually pulverizes the entire single crystal. Increasing the applied current density will lead to higher concentration gradient and higher stress generation. Increasing the cutoff voltage is equivalent to increasing $(C_R - C_0)$ in equation (1). It means higher stress generation and large strain energies at elevated voltages, which causes more "gliding" and "cracking" (Fig. 2). Our findings provide some strategies to stabilize single crystalline Ni-rich NMC by either reducing the crystal size to below 3.5 μm, absorbing accumulated strain energy through modification of the structure symmetry, or simply optimizing the depth of charge without sacrificing much reversible capacity.

References and Notes

1. M. S. Whittingham, Ultimate limits to intercalation reactions for lithium batteries. *Chemical Reiview* **114**, 11414-11443 (2014).
2. J. B. Goodenough, K. S. Park, The Li-ion Rechargeable Battery A Perspective. *Journal of the American Chemical Society* **135**, 1167-1176 (2013).
3. S. Chen *et al.*, Critical Parameters for Evaluating Coin Cells and Pouch Cells of Rechargeable Li-Metal Batteries. *Joule* **3**, 1094-1105 (2019).
4. P. Yan *et al.*, Intragranular cracking as a critical barrier for high-voltage usage of layer-structured cathode for lithium-ion batteries. *Nat Commun* **8**, 14101 (2017).
5. Y. W. Mao *et al.*, High-Voltage Charging-Induced Strain, Heterogeneity, and Micro-Cracks in Secondary Particles of a Nickel-Rich Layered Cathode Material. *Advanced Functional Materials* **29**, (2019).
6. M. M. Besli *et al.*, Mesoscale Chemomechanical Interplay of the $LiNi_{0.8}Co_{0.15}Al_{0.05}O_2$ Cathode in Solid-State Polymer Batteries. *Chemistry of Materials* **31**, 491-501 (2019).
7. R. Jung *et al.*, Effect of Ambient Storage on the Degradation of Ni-Rich Positive Electrode Materials (NMC811) for Li-Ion Batteries. *Journal of the Electrochemical Society* **165**, A132-A141 (2018).

8. K.-W. Nam *et al.*, Combining in situ synchrotron X-Ray diffraction and absorption techniques with transmission electron microscopy to study the origin of thermal instability in overcharged cathode materials for lithium-ion batteries. *Advanced Functional Materials* **23**, 1047-1063 (2013).
9. M. Jo, Y. S. Hong, J. Choo, J. Cho, Effect of $LiCoO_2$ Cathode Nanoparticle Size on High Rate Performance for Li-Ion Batteries. *Journal of the Electrochemical Society* **156**, A430-A434 (2009).
10. H. Y. Li, J. Li, X. W. Ma, J. R. Dahn, Synthesis of Single Crystal $LiNi_{0.6}Mn_{0.2}Co_{0.2}O_2$ with Enhanced Electrochemical Performance for Lithium Ion Batteries. *Journal of the Electrochemical Society* **165**, A1038-A1045 (2018).
11. J. Li *et al.*, Synthesis of Single Crystal $LiNi_{0.5}Mn_{0.3}Co_{0.2}O_2$ for Lithium Ion Batteries. *Journal of the Electrochemical Society* **164**, A3529-A3537 (2017).
12. J. C. Garcia *et al.*, Surface Structure, Morphology, and Stability of $Li(Ni_{1/3}Mn_{1/3}Co_{1/3})O_2$ Cathode Material. *Journal of Physical Chemistry C* **121**, 8290-8299 (2017).
13. T. Kimijima *et al.*, Molybdate flux growth of idiomorphic $Li(Ni_{1/3}Co_{1/3}Mn_{1/3})O_2$ single crystals and characterization of their capabilities as cathode materials for lithium-ion batteries. *Journal of Materials Chemistry A* **4**, 7289-7296 (2016).
14. G. Qian *et al.*, Single-crystal nickel-rich layered-oxide battery cathode materials: synthesis, electrochemistry, and intra-granular fracture. *Energy Storage Materials* **27**, 140-149 (2020).
15. Y. Liu, J. Harlow, J. Dahn, Microstructural Observations of "Single Crystal" Positive Electrode Materials Before and After Long Term Cycling by Cross-section Scanning Electron Microscopy. *Journal of The Electrochemical Society* **167**, (2020).
16. J. E. Harlow *et al.*, A Wide Range of Testing Results on an Excellent Lithium-Ion Cell Chemistry to be used as Benchmarks for New Battery Technologies. *Journal of The Electrochemical Society* **166**, A3031-A3044 (2019).
17. J. Li, H. Y. Li, W. Stone, S. Glazier, J. R. Dahn, Development of Electrolytes for Single Crystal NMC532/Artificial Graphite Cells with Long Lifetime. *Journal of the Electrochemical Society* **165**, A626-A635 (2018).
18. J. Zhu, G. Y. Chen, Single-crystal based studies for correlating the properties and high-voltage performance of $Li[Ni_xMn_yCo_{1-x-y}]O_2$ cathodes. *Journal of Materials Chemistry A* **7**, 5463-5474 (2019).
19. H. Li *et al.*, Synthesis of Single Crystal $LiNi_{0.88}Co_{0.09}Al_{0.03}O_2$ with a Two-Step Lithiation Method. *Journal of The Electrochemical Society* **166**, A1956-A1963 (2019).
20. J. Xiao, "Understanding and Modifying Cathode / Electrolyte Interfaces," DOE VTO Annual Merit Review, 2019.
21. J. M. Zheng, P. F. Yan, L. Estevez, C. M. Wang, J. G. Zhang, Effect of calcination temperature on the electrochemical properties of nickel-rich $LiNi_{0.76}Mn_{0.14}Co_{0.10}O_2$ cathodes for lithium-ion batteries. *Nano Energy* **49**, 538-548 (2018).
22. M. B. Pinson, M. Z. Bazant, Theory of SEI Formation in Rechargeable Batteries: Capacity Fade, Accelerated Aging and Lifetime Prediction. *Journal of The Electrochemical Society* **160**, A243-A250 (2013).
23. T. L. Anderson, *Fracture Mechanics: Fundamentals and Applications*. (CRC Press, ed. Forth, 2017).

24. H. H. Ryu, K. J. Park, C. S. Yoon, Y. K. Sun, Capacity Fading of Ni-Rich $Li[Ni_xCo_yMn_{1-x-y}]O_2$ ($0.6 < x < 0.95$) Cathodes for High-Energy-Density Lithium-Ion Batteries: Bulk or Surface Degradation? *Chemistry of Materials* **30**, 1155-1163 (2018).
25. M. D. Radin, J. Alvarado, Y. S. Meng, A. Van der Ven, Role of Crystal Symmetry in the Reversibility of Stacking-Sequence Changes in Layered Intercalation Electrodes. *Nano letters* **17**, 7789-7795 (2017).
26. A. Ulvestad *et al.*, Topological defect dynamics in operando battery nanoparticles. *Science* **348**, 1344-1347 (2015).
27. J. Xiao, How lithium dendrites form in liquid batteries. *Science* **366**, 426-427 (2019).
28. R. Deshpande, Y. Qi, Y. T. Cheng, Effects of Concentration-Dependent Elastic Modulus on Diffusion-Induced Stresses for Battery Applications. *Journal of the Electrochemical Society* **157**, A967-A971 (2010).

Acknowledgments: The authors thank Q. Li and D. Lu at PNNL for helping electrode preparation and electrochemical tests. **Funding:** This work was supported by the Assistant Secretary for Energy Efficiency and Renewable Energy, Office of Vehicle Technologies of the U.S. Department of Energy through Applied Battery Research Program under Contract No.DE-LC-000L053. E.H. is supported by the Assistant Secretary for Energy Efficiency and Renewable Energy, Vehicle Technology office of the U.S. DOE through the Advanced Battery Materials Research program under contract No. DE-SC0012704. Y.W. and Y.Q. thanks National Science Foundation through grant number DMR-1832808. This research used 28-ID-2 (XPD) of the National Synchrotron Light Source II, a U.S. Department of Energy (DOE) Office of Science User Facility operated for the DOE Office of Science by Brookhaven National Laboratory under Contract No. DE-SC0012704. PNNL is a multiprogram national laboratory operated by Battelle for the DOE under Contract DE-AC05-76RL01830. Part of this work was presented during 2019 DOE Vehicle Technology Office Annual Merit Review Meeting. **Author contributions:** J.X. and Y.B. proposed the research and conceptualized the idea. Y.B. synthesized single crystal samples. Y.B. performed the electrochemical measurements and SEM characterization with help from B.W. and J.H. J.T. conducted the in situ EC-AFM tests and analyzed data. C.W., L.L. and Y.X. collected the TEM data. E.H. collected the synchrotron data and structure refinement. Y.Q. and Y.W. carried out the mechanical modeling. J.Z. participated in data analysis and discussion. Y.B. and J.X. drafted the manuscript with input and revision from all authors. **Competing interests:** The authors declare no competing interests. **Data and materials availability:** All data are available in the main text or the supplementary materials.

Supplementary Materials:

Materials and Methods

Figures S1-S22

Tables S1-S4

Movie S1

References (*29-36*)

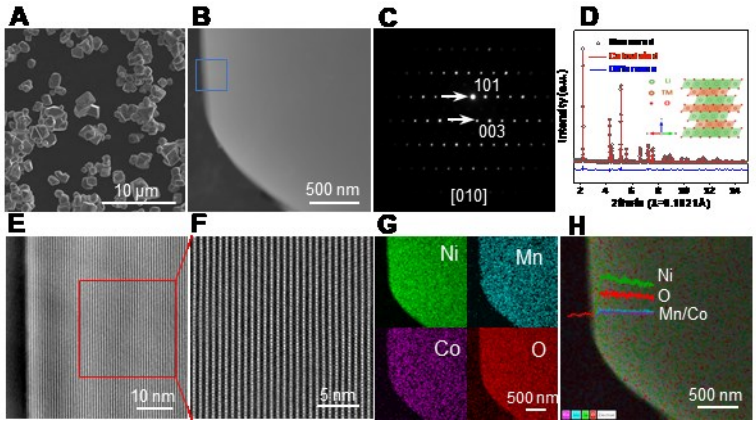

Fig. 1. Characterization of single crystalline $LiNi_{0.76}Mn_{0.14}Co_{0.10}O_2$. (A) SEM image of single crystalline NMC76. (B) Cross-section image of single crystalline NMC76. (C) Selected area electron diffraction pattern of single crystalline NMC76. (D) Synchrotron XRD and Rietveld refinement pattern. (E) High resolution HAADF-STEM image of single crystalline NMC76 (corresponding to blue color square in B). (F) Higher magnification corresponding red color-coded region in E. (G) EDS elemental mapping of Ni, Mn, Co and O. (H) EDS overlapped image and line scanning shows the elemental distribution intensity (the inset).

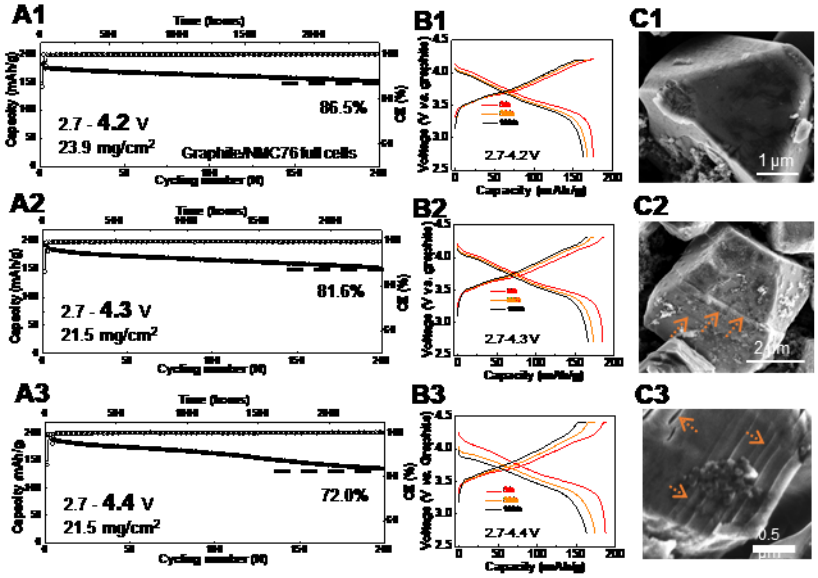

Fig. 2. Electrochemical performance of single crystal $LiNi_{0.76}Mn_{0.14}Co_{0.1}O_2$ and SEM images after cycling stability tests. (A1)(A2)(A3) Cycling stability of single crystalline NMC76 in full cells within different electrochemical windows. (B1)(B2)(B3) The corresponding charge-discharge curves of cells in (A1)(A2)(A3). (C1)(C2)(C3) SEM images of single crystal after 200 cycles in (A1)(A2)(A3).

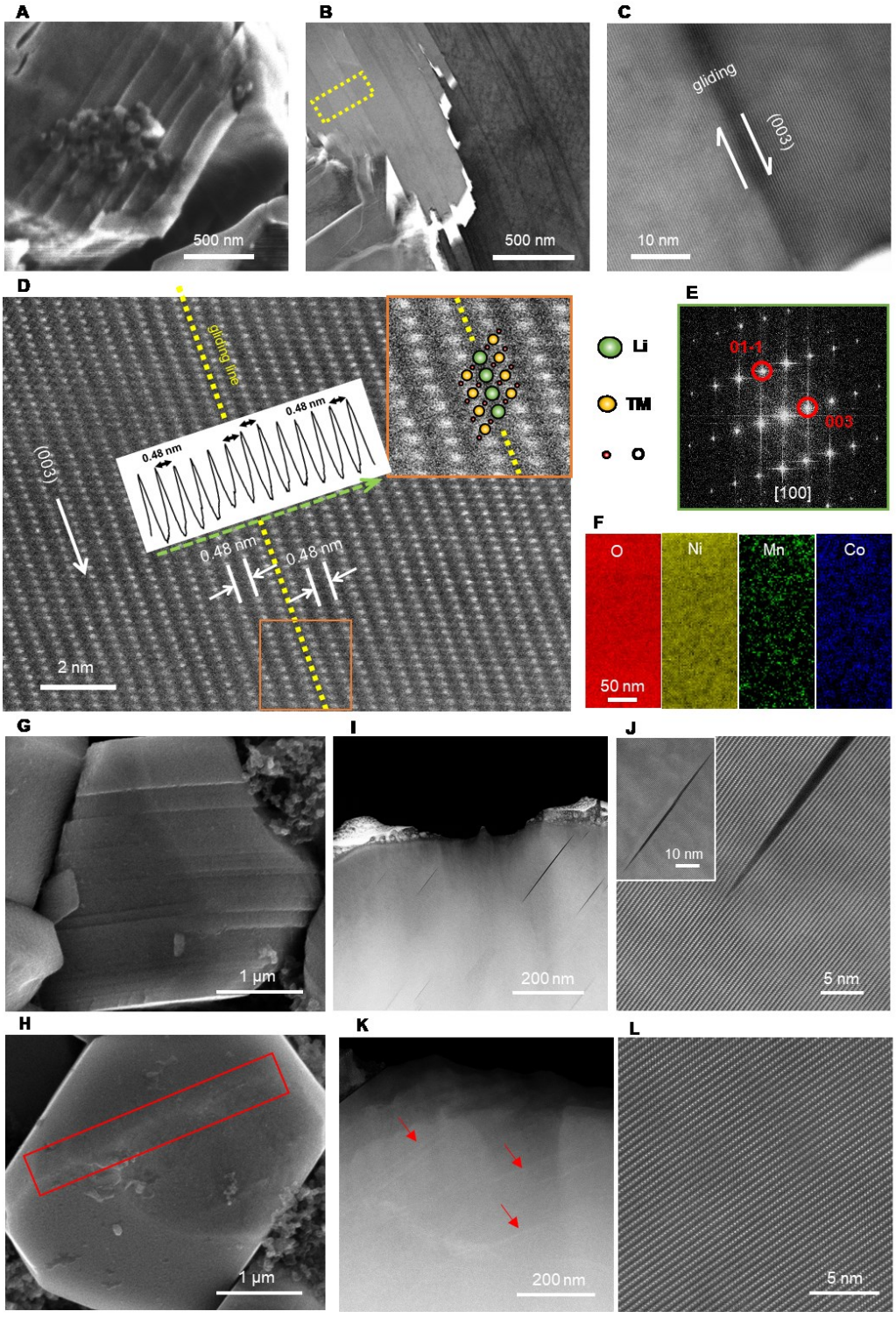

Fig. 3. Morphology and structure study of single crystalline NMC76. (A) SEM image of single crystalline NMC76 after 200 cycles. (B) Cross-section STEM bright field image of single crystalline NMC76 after 200 cycles. (C) STEM bright field image of internal slicing. (D) STEM-

HAADF image around slicing area. Upper inset is zoomed image of slicing area. (E) SAED of gliding area. (F) EELS mapping of selected area in (B). (G) SEM images of single crystalline NMC76 initially charged to 4.8 V (vs. Li^+/Li). (H) SEM images of single crystalline NMC76 discharged to 2.7 V (after being charged to 4.8 V vs. Li^+/Li). (I)(J) STEM images of single crystalline NMC76 at 4.4 V charge status (cycled in a full cell between 2.7-4.4 V for 120 cycles). (K)(L) STEM images of single crystalline NMC76 at discharge status (cycled in full cell between 2.7-4.4 V for 120 cycles).

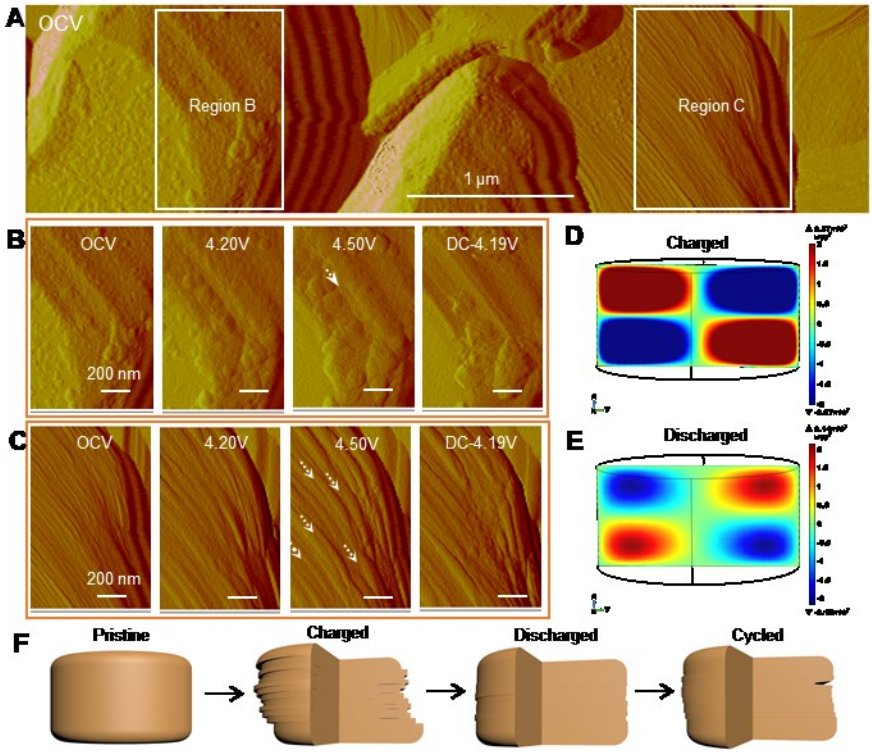

Fig. 4. Surface structure and morphology evolution by in situ AFM and mechanical analysis for single crystalline NMC76. (A) AFM image at OCV state. (B)(C) Comparison of selected surface evolution during in situ AFM testing. (D) COMSOL simulated shear stress along yz direction during charge (delithiation) at scaled time of 0.1T. (E) COMSOL simulated shear stress along yz direction during discharge (lithiation) at scaled time of 0.1T. (F) Schematic illustration of structural evolution of single crystalline NMC76 upon cycling.